Final Draft
of the original manuscript:

Yang, L.; Huang, Y.; Feyerabend, F.; Willumeit, R.; Mendis, C.; Kainer, K.U.; Hort, N.:

Microstructure, mechanical and corrosion properties of Mg–Dy–Gd–Zr alloys for medical applications

In: Acta Biomaterialia (2013) Elsevier

DOI: 10.1016/j.actbio.2013.03.017

Microstructure, mechanical and corrosion properties of Mg-Dy-Gd-Zr alloys for medical applications

Lei Yang*, Yuanding Huang, Frank Feyerabend, Regine Willumeit, Chamini Mendis, Karl Ulrich Kainer, Norbert Hort

Helmholtz Zentrum Geesthacht, Institute of Materials Research, Max-Planck-Str. 1, D-21502 Geesthacht, Germany

Abstract

In previous investigations Mg-10Dy (wt.%) alloy with a good combination of corrosion resistance and cytocompatibility showed a great potential for the use as biodegradable implant material. However, the mechanical properties of Mg-10Dy alloy are not satisfactory. In order to allow the tailoring of mechanical properties required for various medical applications, four Mg-10(Dy+Gd)-0.2Zr (wt.%) alloys were investigated with respect to microstructure, mechanical and corrosion properties. With the increase of Gd content, the amount of second phase particles increased in the as-cast alloys and the age hardening response increased at 200 °C. The yield strength increased while the ductility reduced especially for peak-aged alloys with the addition of Gd. Additionally, with increasing Gd content, the corrosion rate increased in the as-cast condition due to galvanic effect, but all the alloys have a similar corrosion rate (about 0.5 mm/year) in solution treated and aged condition.

Keywords: Mg-Dy-Gd-Zr alloys, Microstructure, Mechanical properties, Corrosion properties

* Corresponding author Address:

Helmholtz Zentrum Geesthacht, Magnesium Innovation Centre, Institute of Materials Research, Max-Planck-Str. 1, D-21502 Geesthacht, Germany; E-mail address: lyang0522@gmail.com

1 Introduction

Mg alloys have attracted much attention for their potential use in medical applications due to the low Young's modulus (40-45 GPa) compared with Ti alloys (Ti6Al4V, 114 GPa) and stainless steels (193 GPa), appropriate strength compared to bone, good biodegradability and bioresorbability [1-3]. Even though Mg and its alloys have been investigated as implants for almost two centuries, implants of Mg and its

alloys are yet to be commercialized. One of the key issues preventing this is that Mg and its alloys would lose mechanical integrity before the sufficient healing of body tissues, which can be caused by low mechanical properties, high corrosion rate and localized corrosion [1]. One of the effective approaches to overcome this is the use of alloying elements and heat treatments to enhance mechanical properties and corrosion resistance but eliminate localized corrosion behaviour.

Many Mg-based alloy systems, such as Mg-Ca [4, 5], Mg-Zn [6, 7], Mg-Sr [8-10], Mg-Y [11], Mg-RE (RE = rare earth) [12-15] systems, are proposed for medical applications. Mg alloys containing RE elements, such as WE43 (Mg-4Y-3RE, wt.%) and AE42 (Mg-4Al-2RE, wt.%), have already shown a good combination of mechanical and corrosion properties in structural application. This has led to a continuous evaluation of RE-containing Mg alloys for medical applications. *In vivo* studies on LAE442 (Mg-4Li-4Al-2RE, wt.%) alloy for orthopedics applications show that it has low corrosion rate and has an acceptable host response [16-18]. The more advanced applications are biodegradable cardiovascular stents made of Mg-RE alloys. Heublein et al. [19] reported on the degradation of AE21 (Mg-2Al-1RE, wt.%) in a coronary artery and concluded that the vascular implants made of Mg alloys seemed to be a realistic alternative to permanent implants. Moreover, several clinical human trials have been conducted with biodegradable stents made of Mg-RE, and it is found that the Mg-RE stents had good biocompatibility but the combination of mechanical and corrosion properties needs further improvement [20, 21]. Mg-RE alloy was the only Mg alloy used in clinical trials reported to date [21]. These previous investigations indicate that some of the RE-containing Mg alloys are promising candidates for degradable biomaterials.

Previous work has shown that Mg-10Dy alloy has a low corrosion rate, uniform corrosion behavior and good cytocompatibility [22, 23]. However, the mechanical properties of Mg-10Dy alloy are not satisfactory. Moreover, Mg-10Dy alloy shows no age hardening response during ageing [24], which limits the potential for tailoring mechanical properties by heat treatment. Gd has similar chemical properties but better age hardening response compared with Dy [25, 26]. Based on earlier research [15, 27] the use of Gd as alloying elements seems to be suitable. Furthermore, Gd-based contrast agents are widely used as the contrast medium in magnetic resonance imaging as the biocompatibility of Gd is acceptable [28-30]. Therefore, Mg-10(Dy+Gd)-0.2Zr alloys are developed in this work to enhance the age hardening

response and to tailor the mechanical properties through replacing some of the Dy in Mg-10Dy alloy with Gd. The addition of Gd is expected to potentially improve age hardening response while reduce the ductility. Meanwhile, the total amount of Dy and Gd is set at 10wt% to maintain the corrosion resistance. A small amount of Zr was added in the alloys as grain refinement agent to obtain homogeneous microstructure.

2 Experimental procedure

2.1 Material preparation

Mg-10(Dy+Gd)-0.2Zr alloys were designed and their nominal chemical composition is listed in Table 1. High-purity Mg (Magnesium Elektron, UK, 99.94%) was molten in a mild steel crucible under a protective atmosphere (Ar + 2% SF_6). Pure Dy (Grirem, Beijing, China, 99.5%), pure Gd (Grirem, Beijing, China, 99.5%) and Mg-33 wt.% Zr master alloy (Magnesium Elektron, UK) were added to the melt at 720 °C in the nominal amount. The melt was stirred for 30 min at 200 rpm and then poured into a mould preheated to 500 ^{o}C. The filled mould was held at 670 ^{o}C for 30 min under the protective gas to let the heavy impurities settle to the bottom and let the light impurities float up to the top of the ingots. Then permanent mould direct chill casting [31] was used to prepare the alloys. The size of ingots is Ø12cm×20cm. After casting both the bottom and top of the ingots were cut away, and the middle parts were used for further investigations. Solution treatment (T4) was carried out at 520°C for 8 h followed by water quenching. Ageing treatment (T6) was performed at 200 °C for various times followed by air cooling.

The chemical composition of the alloys and impurities were analyzed using a X-ray fluorescence (XRF) analyzer (Bruker AXS S4 Explorer, Germany) for Dy, Gd, Zr and Ni, and using spark optical emission spectroscopy (Spectrolab M9 Kleve, Germany) for Fe and Cu. The content of Ni could not be determined with spark optical emission spectroscopy due to interference of strong Dy peaks. Therefore, the Ni content was determined from the XRF results. The content of Zr at the bottom of the ingots (the cut away part) was also measured using XRF.

2.2 Microstructure analysis

Specimens were ground using silicon carbide emery paper up to 2500 grit, and mechanically polished. Optical microstructure was characterized using a light

microscope (Reichert-Jung MeF3, Germany) with a polarization system. Grain sizes were determined using the line intercept method [32]. For scanning electron microscopy (SEM), specimens were electropolished using an electrolytic apparatus (LectroPol-5, Struers Inc). A Zeiss Ultra 55 (Carl Zeiss GmbH, Oberkochen, Germany) SEM, operating at 15kV, equipped with energy dispersive X-ray spectroscopy (EDX) was used to observe the microstructure.

Transmission electron microscopy (TEM) specimens were ground mechanically to about 120 μm and then thinned with twin jet electropolishing in a solution of 2.5 % $HClO_4$ and 97.5 % ethanol at about −45 °C and a voltage of 40 V. The TEM examinations were carried out on a Philips CM 200 operating at 200 kV.

For the phase analysis, X-ray diffraction (XRD) measurements were performed using a diffractometer (Siemens D5000, Germany) with Cu K-α_1 radiation (wavelength λ = 0.15406 nm) and a secondary monochromator. The step size was 0.02 ° and the time at each step was 3 s. CaRIne crystallography software (version 3.1) was used to simulate the diffraction peak of β′ phase based on its crystal structure (orthorhombic, a = 0.64, b = 0.22, c = 0.52) [33, 34].

2.3 Mechanical tests

Hardness measurements were carried out using a Vickers hardness test machine (Karl Frank GMBH, Germany) with a load of 5 kg and a dwelling time of 10 seconds. Ten points were averaged for each test condition. Tension and compression tests were performed at room temperature using a Zwick 050 testing machine (Zwick GmbH & Co., KG, Ulm, Germany) according to DIN EN 10002 [35] and DIN 50106 [36]. Tensile specimens with a gauge length of 30 mm, a diameter of 6 mm and threaded heads of 10 mm were used. The compression specimens were cylinders with a height of 16.5 mm and a diameter of 11 mm. Both tension and compression tests were done at a strain rate of 1×10^{-3} s^{-1}. A minimum of three specimens were tested for each condition.

2.4 Corrosion

Weight loss tests were performed in a cell culture medium (CCM) under cell culture conditions (37°C, 21% O_2, 5% CO_2, 95% rH). The CCM consists of Dulbecco's modified eagle medium (DMEM, Life Technologies, Darmstadt, Germany) and 10% fetal bovine serum (FBS, PAA Laboratories, Linz, Austria). Composition of the DMEM

can be found elsewhere [23]. Compared with simulated body fluid and Hank's solution the composition of CCM is closer to the real body fluid. The cell culture conditions are more similar to *in vivo* environment. The specimens with a size of 10 × 10 × 10 mm^3 were prepared by grinding each side with 2400 grid emery paper and degreasing the surfaces with ethanol prior to corrosion tests. For the corrosion tests in CCM, the specimens were sterilized in 70% ethanol for 15 min before the corrosion tests and all subsequent procedures were carried out under sterile conditions. The specimens were immersed in CCM with a ratio of 1.5 ml / cm^2 for 14 days. Corrosion products were removed via immersing the specimens in chromic acid (180 g/l) for 20 min at room temperature. The average corrosion rate was calculated in millimetre per year (mm/y) using the following equation [37]:

$$CR = \frac{8.76 \times 10^4 \times \Delta \mathrm{g}}{\mathrm{A} \cdot t \cdot \rho}$$

where Δg is weight change in g, A is surface area in cm^2, t is immersion time in hours (h) and ρ is density of the alloy in $g \cdot cm^{-3}$. At least three specimens were tested for each condition. In order to understand the corrosion mechanism, the corrosion morphology was examined.

3 Results

3.1 Chemical compositions

Table 2 shows the experimentally measured composition of Mg-Dy-Gd-Zr alloys. The loss of alloying elements is around 10-20% for Gd and Dy, but is much higher for Zr (around 85%). Only ~0.03 wt.% Zr was detected in the middle part of the ingots. However, the content of Zr at the bottom of the ingots (the part cut away) is around 1 wt.%, which is much higher than its nominal content (0.2 wt.%). No Ni content was detected using XRF. Since the detection limit of Ni for the used XRF instrument is 0.004 wt.%, the content of Ni is less than 0.004 wt.%.

3.2 Microstructure and phase characterization

Optical microstructures were similar for all alloys investigated, thus only the microstructures of DG28K alloy in the as-cast and the T4 conditions are shown (Fig. 1). A homogeneous distribution of equiaxed grains were observed in both as-cast and T4 condition. All the alloys have a similar grain size (around 60 μm) in the as-cast condition, and they did not coarsen following the T4 treatment (Fig. 2). The typical

dendritic structure observed in the as-cast condition disappeared after T4 treatment.

The SEM analysis showed that the microstructures of the as-cast alloys consisted of Mg matrix, segregation area of alloying elements and second phase particles as indicated by arrows in Fig. 3. The segregation of alloying elements (bright bands) is mainly located at the interdendritic region and the grain boundaries. All second phase particles are distributed in the segregation area. For D10K and DG82K alloy, only very few and small (nano-scale) second phase particles are observed (Fig. 3 (a, b)). When the amount of Gd is increased, both the volume fraction and size of second phase particles increase (Fig. 3 (c, d)).

The distribution of alloying elements in the α-Mg matrix, segregation area and second phase particles was analyzed by EDX, as listed in Table 3. With the increase in Gd, Dy content reduced and Gd content increased in all the areas, while the total amount of alloying elements in the matrix and segregation area decreased. For example, in the segregation area the amount of alloying elements is around 19.6 wt.% and 15.5 wt.% for D10K and DG28K alloys, respectively. Since the second phase particles in D10K and DG28K alloy are very small (< 1 μm), EDX analysis could not be carried out properly. Thus, only the phase compositions for DG55K and DG28K are shown in Table 3. Both Dy and Gd are found in the second phase particles, while the Gd amount is much higher than Dy. For example, Gd (32.5 wt.%) is more than twice that of Dy (14.6 wt.%) in the DG55K alloy, although Gd and Dy are equally available. In the second phase particles, although the amount of Dy and Gd changes with the change in alloy compositions, the total amount of them is similar (around 57 wt.% / 14 at.%).

Fig. 4 shows the SEM microstructure of alloys after T4 treatment. The segregation region is disappeared completely. Almost all of the second phase particles are dissolved into the matrix for D10K and DG82K alloys (Fig. 4 (a, b)), while a few very small second phase particles can be found in the DG55K and DG28K alloys (Fig. 4 (c, d)). The remaining second phase particles mainly distribute along the grain boundaries (Fig. 4 d)).

To investigate the age hardening response of Mg-10(Dy+Gd)-0.2Zr alloys, Vickers hardness was measured after ageing for different times at 200 °C (Fig. 5). By comparing the Vickers hardness of different alloys after ageing for same length of time, the age hardening response increases with the increased Gd. For D10K alloy, there is little age hardening response. For DG82K and DG55K alloys, 64.4 and 85.5

Hv of peak hardness is obtained after 216 h aging, respectively. While for DG28K alloy, 100.2 Hv of peak hardness is obtained only after 72 h aging. There are plateaus of peak-ageing region from 210 h to 384 h and from 72 to 120 h for DG55K and DG28K alloys, respectively. Further ageing led to a slow decrease in the hardness.

Since DG28K alloy showed the highest age hardening response, it was selected for the precipitation observation using TEM. Fig. 6 presents the TEM micrographs of precipitates and their selected area diffraction pattern recorded from DG28K alloy at peak aged condition (200°C / 72 h). Large number of precipitates distributed uniformly in the matrix (Fig. 6 (a, c)). The additional reflections were observed on the selected area diffraction pattern with the incident electron beam approximately parallel to $\langle \bar{1}2\bar{1}3 \rangle_{\alpha}$ and $[0001]_{\alpha}$ (Fig. 6 (b, d)). These additional reflections can be indexed according to metastable β′ phase which has a composition close to $Mg_{13}RE_3$ and a base-centered orthorhombic structure (a = 0.64 nm, b = 2.22 nm, c = 0.52 nm) [33, 34, 38, 39]. The orientation relationship between β′ and Mg matrix phase is $[001]_{\beta'}$ // $[0001]_{\alpha}$ and $(100)_{\beta'}$ // $(1\bar{2}10)_{\alpha}$ [38]. In peak-aged condition at 200 °C, β′ precipitates were also observed as the dominant precipitates in other Mg-RE alloys [34, 40].

As DG28K alloy showed the highest amount of second phase particles in the as cast condition and the most apparent age hardening response, it was selected for the XRD phase analysis. Fig. 7 shows the XRD pattern of DG28K alloy in different conditions. Mg_5RE and β′ phase are identified in the as-cast and peak aged condition, respectively. This is consistent with the phase analysis results using EDX and TEM.

3.3 Mechanical properties

Fig. 8 presents the mechanical properties obtained in tension and compression tests. The tensile yield strength (TYS) and ultimate tensile strength (UTS) of alloys in different conditions are shown in Fig. 8 (a, b). In the as-cast condition, the TYS and UTS improved slightly with the increase in Gd, and they increase by around 17 MPa and 29 MPa respectively when Gd is increased from 0 (D10K) to 8 wt.% (DG28K). T4 treatment did not alter the TYS and UTS. After T6 treatment, the TYS and UTS still remained unchanged for D10K and DG82K alloys, while they increase apparently for DG55K and DG28K alloys. For example, the TYS and UTS increased by 96 MPa and 140 MPa for DG28K alloy.

The tensile elongation of alloys in different conditions is shown in Fig. 8 (c). In the as-cast condition, the tensile elongation reduces gradually with the increase of Gd content, reducing from 21% to 17.6% when Gd content is increased from 0 (D10K) to 8wt.% (DG28K). After T4 treatment, the tensile elongation increased marginally for all alloys. After T6 treatment, the elongation reduced slightly for D10K and DG82K alloys, whereas in DG55K and DG28K alloys a dramatic decrease can be observed (e.g. from 18.3% to 7.5% for DG28K alloy).

A similar trend to that observed for tensile properties is found for the compressive properties of Mg-Dy-Gd-Zr alloys (Fig. 8). In the as-cast conditions, the increase in Gd led to a slight increase in both the CYS and the UCS, and a decrease in the compressibility to failure. T4 heat treatment did not change the CYS and compressibility (Fig. 8 (d, f)), while it reduces the UCS for all alloys investigated (Fig. 8 e). The UCS reduced from 350 MPa to 290 MPa for DG28K alloy following the T4 heat treatment (Fig. 8 e). After the T6 treatment, the CYS, UTS and compressibility to failure marginally changed for the D10K and DG82K alloys (Fig. 8 (d, e, f)). The CYS increases for DG55K and DG28K alloys while a large reduction in the compression to failure is observed (Fig. 8 (d, f)). The UCS increases only for the DG28K alloy following the T6 heat treatment (Fig. 8 e).

3.4 Corrosion properties

Fig. 9 shows the corrosion rate of alloys after immersion in CCM for 14 days under cell culture conditions. In the as-cast condition, the corrosion rate for D10K and DG82K alloys is similar (about 0.55 mm/year). The corrosion rate increased to 0.7 and 0.85 mm/year when Gd content increases to 5 and 8 wt.% in DG55K alloy and DG28K alloy. After T4 treatment, the corrosion rate has little change for D10K and DG82K alloy, while it reduced to around 0.5mm/year for DG55K and DG28K alloys. As a result, all the alloys had a similar corrosion rate in T4 condition. Aging treatment had no adverse influence on the corrosion rate, and even reduced it slightly.

To check the corrosion type of the studied alloys, the macro corrosion morphologies of weight loss tests samples (after removal of corrosion products) were recorded as presented in Fig. 10. In the as-cast condition, localized corrosion occurs on the surface of all alloys as indicated by arrows. The localized corrosion becomes increasingly serious with the increase of Gd. In the T4 and T6 conditions, no localized corrosion is found and the corrosion is very uniform.

4 Discussion

4.1 Chemical compositions

The Zr content is low (around 0.03 wt.%) in the middle part of the ingots and is very high at the bottom of the ingots (around 1 wt.%). This can be attributed the following reasons. Before the final casting, the melt was held for 30 minutes without stirring. During this time, firstly Zr can react with impurities such as Fe and Ni and form compounds [41]. Due to their density (much higher than those of the Mg melt) they settle and deposit at the bottom of the ingots. Secondly, if Zr is not reacting with alloying elements or impurities it forms metallic Zr particles in a peritectic reaction during solidification or holding at the given temperatures [42, 43]. Zr has a density of 6.5 g cm^{-3}. As long as a melt is not stirred properly, metallic Zr particles will form, grow and they will settle.

4.2 Microstructure and age hardening behavior

Based on the Mg–Dy and Mg-Gd binary phase diagrams [44] (Fig. 11), the maximum solid solubility of Dy (25.3 wt.%) and Gd (23.5 wt.%) in Mg matrix are similar at eutectic temperature. However, their solid solubility decreases at different rates with the decrease in temperature. The solid solubility of Dy reduces gradually with the decrease in temperature and reach to ~10 wt.% at 200 °C (Fig. 11 a). In contrast, the solid solubility of Gd in Mg reduces dramatically with the decrease in temperature, and reaches to ~3wt.% at 200 °C (Fig. 11 b). As a result, the driving force for precipitation is higher with Gd than Dy additions. This could be the reason that in the as-cast condition the amount of second phase particles increase with the increase in Gd amount in alloys, despite the total amount of alloying elements remain constant (Fig. 3). According to the EDX and XRD analysis, the second phase particles in DG55K and DG28K alloys are approximately $Mg_5(Dy+Gd)$ phases and the Dy and Gd content depends on the Dy and Gd content in the alloys. In general, Mg_5RE could be formed in Mg-Dy, Mg-Gd and Mg-Y based Mg-RE alloys [45]. The ratio of the rare earth elements present in the second phase particles varies in different alloys. It is reported that $Mg_5(Nd_{0.5}Gd_{0.5})$, $Mg_5(Nd_{0.7}Dy_{0.3})$ and $Mg_5(Nd_{0.33}Y_{0.67})$ are formed in Mg-7Gd-2Nd, Mg-7Dy-2Nd and Mg-4Y-2Nd alloys respectively [45].

The solubility of Dy and Gd in α-Mg matrix is 22 wt.% and 19wt.% at 520 °C,

respectively (Fig. 11), suggesting complete dissolution of Dy- and Gd-containing second phase particles into α-Mg matrix during solid solution treatment. However, a few fine second phase particles were found in DG55K and DG28K alloys after solid solution at 520 °C for 8 hours. During solution treatment, the composition homogenization occurs by the diffusion of Dy and Gd from the regions near grain boundaries to the centre of the grains. The annealing time during which the second phase particles can completely dissolve depends on the size of particles and the diffusion rate of alloying elements. It is reported that the diffusion rate of RE elements in solid Mg matrix is slow [46]. Even after solution treatment at 525 °C for 24 hours, a few Mg_5Gd phases is still left in Mg-15wt.%Gd alloy [15]. Therefore, the remained second phase particles in DG55K and DG18K alloys can be attributed to the slow diffusion rate of RE in solid Mg.

No age hardening response was observed for D10K alloy. This is due to the high solubility (~ 10wt.%) of Dy at 200 °C in Mg matrix, causing all the Dy to remain in the α-Mg matrix rather than form precipitates. As mentioned, Gd has a lower solubility (~ 3wt.%) than Dy at 200 °C. Thus, Gd has higher driving force to form precipitates than Dy in Mg-Dy-Gd-Zr alloys during ageing. With the increase in Gd content in Mg-Dy-Gd-Zr alloys, the amount of β′ precipitates increased and the age hardening behaviour becomes more significant. An enhanced age hardening response is obtained with Gd addition. Apps et al. [26] investigated the age hardening behaviour of Mg-7Dy-2Nd and Mg-7Gd-2Nd alloys, and they also found that Gd is more effective in strengthening than Dy. The peak Vickers hardness of 104 Hv was achieved for the Mg-7Gd-2Nd alloy, while it only reached 86 Hv for Mg-7Dy-2Nd alloy.

4.3 Mechanical properties

In the as-cast alloys, Hall–Petch strengthening, solid solution strengthening as well as precipitation strengthening contributes to the total strength. After T4 treatment, precipitation strengthening is negligible as only very few particles remain in the α-Mg matrix. The Hall–Petch strengthening is similar in all alloys due to the similar grain sizes. As a result, solid solution strengthening is the only factor which contributes to the different values of hardness and yield strength observed. The total amount of alloying elements in the alloys is similar, but with the increase in Gd the hardness and yield strength increase. This indicates Gd has a better solution strengthening effect than Dy. The Vickers hardness of Mg-7Gd-2Nd alloy is 20% higher than that of Mg-

7Dy-2Nd alloy in T4 condition [26].

During T6 treatment, the decomposition of the supersaturated α-Mg solid solution occurs and β′ precipitates form (Fig. 6). These precipitates block dislocation movement and contribute to precipitation strengthening. The high density of intrinsically strong, plate-shaped precipitates with prismatic habit planes and large aspect ratios contributes to significant precipitation strengthening [47]. Consequently, higher increase in yield strength was obtained after T6 treatment with the increase of Gd, as listed in Table 4. However, these precipitates deteriorate the ductility of the alloys and both of the tensile elongation and compressibility reduced after T6 treatment, especially for DG28K alloy in which large amount of β′ precipitates were observed (Table 4).

4.4 Corrosion

In this work, the corrosion rate and localized corrosion increases (Fig. 9 and Fig. 10) with the increase in second phase particles in the alloys (Fig. 3). This is attributed to the galvanic corrosion effects between the second phase particles and α-Mg matrix. Although the electrochemical potential of Mg_5(Dy+Gd) phase is not reported to date, it is reported that corrosion of Mg-Gd and Mg-Dy alloys is accelerated by Mg_5Gd and $Mg_{24}Dy_5$ phase, respectively [15, 22]. Moreover, in Mg-Gd-Y alloys Mg_5(Gd+Y) intermetallics act as cathode and form galvanic corrosion couples with α-Mg matrix, accelerating corrosion [48, 49]. Therefore, it can be deduced that the second phase particles in Mg-Dy-Gd-Zr also form galvanic corrosion cells with α-Mg matrix and this is consistent with the corrosion morphology (Fig. 10).

The negative electrochemical potentials of the elements Dy and Gd are 2.35 V and 2.4 V, which are close to that of Mg (-2.37 V). This indicates that the Dy and Gd would not cause micro-galvanic corrosion with the Mg matrix if it is in solution. After T4 treatment, only very few and small precipitates remain in the α-Mg matrix (Fig. 4). Thus the galvanic corrosion is significantly reduced, which eliminates the localized corrosion of all alloys (Fig. 10). After T6 treatment, large number of β′ precipitates are distributed in the matrix especially for DG28K alloy. However, these β′ precipitates show no adverse effect on the corrosion rate. In CCM, a protective corrosion film forms on the surface of Mg alloys during corrosion [23]. Moreover, organic materials such as proteins would be adsorbed on the surface of the corrosion film [23]. This composite corrosion film could significantly reduce the penetration of Cl^- across the

corrosion interface between the fresh alloy surface and the corrosion film [50, 51], and hence inhibit the tendency of galvanic corrosion. By comparing the corrosion rate of high purity Mg, Mg-9Al-Zn, Mg-4Zn-1RE and Mg-2Zn-0.2Mn alloys in Hank's solution, it is found the galvanic tendency is only weakly influenced by second phase particles [52]. This is attributed to the formation of protective corrosion film on the surface. Another factor affecting the tendency of local micro galvanic corrosion is the cathode to anode area, depending on the size of second phase particles. Compared with the micro-sized second phase particles in the as-cast alloys, the nano-sized precipitates in the aged alloys are much smaller. This largely decreases the local micro galvanic corrosion tendency. No localized corrosion forms in the aged alloys (Fig. 10). Therefore, the possible micro galvanic corrosion between the β' precipitates and Mg matrix is inhibited due to the protective corrosion film and the small size of the β' precipitates. The similar corrosion behavior is observed for T4 treated and T6 treated alloys.

The degradation rate of the heat treated Mg-Dy-Gd-Zr alloys is always in the range from 0.3 to 0.5 mm/year. In the previous work with the same corrosion conditions [23], the degradation rate of pure Mg and Mg-10Dy alloy is found to be around 0.78 mm/y and 0.55 mm/y, respectively. Krikland et al. [53] investigated the degradation rate of a range of Mg alloys in Eagle's essential medium (Invitrogen) under cell culture conditions. The lowest corrosion rate (0.6 mm/y) is observed for AZ91 and Mg-3Zn alloys while the highest corrosion rate reaches to around 60 mm/y for Mg-5Ca alloy. Fe and Fe alloys are also considered to be promising as biodegradable implants, which have a range of *in vitro* corrosion rate from 0.03 to 0.5 mm/y in simulated body fluid [54-56]. The Fe alloys with a high corrosion rate are proposed as potential candidates for further investigations. This is because previous study shows that the degradation rate of pure Fe is too slow as biodegradable stents [57, 58]. Compared with the in vitro degradation rates of other potential biodegradable alloys, the investigated Mg-Dy-Gd-Zr alloys show a very promising future as biodegradable implants.

5 Summary

The mechanical properties of Mg-10(Dy+Gd)-0.2Zr alloys can be tailored in a wide range by adjusting the alloy compositions and heat treatments. The TYS can be

varied between 99.8 and 211.6 MPa. The elongation to fraction is at a minimum value of around 7.8%, while it reaches a maximum value at 24.1%. In addition, all the alloys show a uniform corrosion and a corrosion rate of 0.5 mm/y in the solution treated and aged condition. Therefore, for different medical applications different alloy compositions and heat treatment technique can be selected, which depends on the mechanical properties required.

Acknowledgement

The authors express their gratitude to Prof. R. Schmid-Fetzer and Dr. A. Srinivasan for thoughtful discussions. Thanks to Mr. W. Punessen and Mrs. G. Salamon for excellent technique support. The sponsorship of CSC-Helmholtz scholarship is acknowledged.

References

[1] Staiger MP, Pietak AM, Huadmai J, Dias G. Magnesium and its alloys as orthopedic biomaterials: A review. Biomaterials 2006;27:1728-34.

[2] Witte F, Hort N, Vogt C, Cohen S, Willumeit R, Kainer KU, Feyerabend F. Degradable biomaterials based on magnesium corrosion. Current Opinion in Solid State and Materials Science 2008;12:63-72.

[3] Loos A, Rohde R, Haveich A, Barlach S. In vitro and in vivo biocompatibility testing of absorbable metal stents. Macromol. Symp. 2007;253:103-08.

[4] Li ZJ, Gu XN, Lou SQ, Zheng YF. The development of binary Mg-Ca alloys for use as biodegradable materials within bone. Biomaterials 2008;29:1329-44.

[5] Erdmann N, Angrisani N, Reifenrath J, Lucas A, Thorey F, Bormann D, Meyer-Lindenberg A. Biomechanical testing and degradation analysis of MgCa0.8 alloy screws: A comparative in vivo study in rabbits. Acta Biomater.;7:1421-28.

[6] Zhang S, Zhang X, Zhao C, Li J, Song Y, Xie C, Tao H, Zhang Y, He Y, Jiang Y, Bian Y. Research on an Mg-Zn alloy as a degradable biomaterial. Acta Biomater. 2010;6:626-40.

[7] Zhang E, Xu L, Yu G, Pan F, Yang K. In vivo evaluation of biodegradable magnesium alloy bone implant in the first 6 months implantation. J. Biomed. Mater. Res. 2009;90A:882-93.

[8] Brar HS, Wong J, Manuel MV. Investigation of the mechanical and degradation properties of Mg-Sr and Mg-Zn-Sr alloys for use as potential biodegradable implant materials. Journal of the Mechanical Behavior of Biomedical Materials
7th TMS Symposium on Biological Materials Science 2012;7:87-95.

[9] Li Y, Wen C, Mushahary D, Sravanthi R, Harishankar N, Pande G, Hodgson P. Mg-Zr-Sr alloys as biodegradable implant materials. Acta Biomater. 2012;8:3177-88.

[10] Gu XN, Xie XH, Li N, Zheng YF, Qin L. In vitro and in vivo studies on a Mg-Sr binary alloy system developed as a new kind of biodegradable metal. Acta Biomater. 2012;8:2360-74.

[11] Hanzi AC, Gerber I, Schinhammer M, Loffler JF, Uggowitzer PJ. On the in vitro and in vivo degradation performance and biological response of new biodegradable Mg-Y-Zn alloys. Acta Biomater. 2010;6:1824-33.

[12] Zhang X, Yuan G, Niu J, Fu P, Ding W. Microstructure, mechanical properties, biocorrosion behavior, and cytotoxicity of as-extruded Mg-Nd-Zn-Zr alloy with different extrusion ratios. Journal of the Mechanical Behavior of Biomedical Materials 2012;9:153-62.

[13] Wang YP, Zhu ZJ, He YH, Jiang Y, Zhang J, Niu JL, Mao L, Yuan GY. In vivo degradation behavior and biocompatibility of Mg-Nd-Zn-Zr alloy at early stage. International Journal of Molecular Medicine 2012;29:178-84.

[14] Seitz J-M, Eifler R, Stahl J, Kietzmann M, Bach F-W. Characterization of MgNd2 alloy for potential applications in bioresorbable implantable devices. Acta Biomater. 2012;8:3852-64.

[15] Hort N, Huang Y, Fechner D, Stomer M, Blawert C, Witte F, Vogt C, Drüker H, Willumeit R, Kainer KU, Feyerabend F. Magnesium alloys as implant materials - Principles of property design for Mg-RE alloys. Acta Biomater. 2010;6:1714-25.

[16] Witte F, Kaese V, Haferkamp H, Switzer E, Meyer-Lindenberg A, Wirth CJ, Windhagen H. In vivo corrosion of four magnesium alloys and the associated bone response. Biomaterials 2005;26:3557-63.

[17] Witte F, Fischer J, Nellesen J, Crostack HA, Kaese V, Pisch A, Beckmann F, Windhagen H. In vitro and in vivo corrosion measurements of magnesium alloys.

Biomaterials 2006;27:1013-18.
[18] Witte F, Fischer J, Nellesen J, Vogt C, Vogt J, Donath T, Beckmann F. In vivo corrosion and corrosion protection of magnesium alloy LAE442. Acta Biomater. 2010;6:1792-99.
[19] Heublein B, Rohde R, Kaese V, Niemeyer M, Hartung W, Haverich A. Biocorrosion of magnesium alloys: a new principle in cardiovascular implant technology? Heart 2003;89:651-56.
[20] Zartner P, Cesnjevar R, Singer H, Weyand M. First successful implantation of a biodegradable metal stent into the left pulmonary artery of a preterm baby. Catheter. Cardiovasc. Interv. 2005;66:590-94.
[21] Hermawan H, Dubé D, Mantovani D. Developments in metallic biodegradable stents. Acta Biomater. 2010;6:1693-97.
[22] Yang L, Huang Y, Peng Q, Feyerabend F, Kainer KU, Willumeit R, Hort N. Mechanical and corrosion properties of binary Mg–Dy alloys for medical applications. Materials Science and Engineering: B 2011;176:1827-34.
[23] Yang L, Hort N, Laipple D, Hoeche D, Huang Y, Kainer KU, Willumeit R, Feyerabend F. Element distribution in corrosion layer and cytotoxicity of Mg-10Dy alloy during *in vitro* bio-degradation. Acta Biomater. Accepted.
[24] Yang L, Huang Y, Feyerabend F, Willumeit R, Kainer KU, Hort N. Influence of ageing treatment on microstructure, mechanical and bio-corrosion properties of Mg-Dy alloys. Journal of the Mechanical Behavior of Biomedical Materials 2012;13:36-44.
[25] Dean JA, editor Lange's Handbook of Chemistry: GcGraw-Hill, 1999.
[26] Apps PJ, Karimzadeh H, King JF, Lorimer GW. Precipitation reactions in magnesium-rare earth alloys containing Yttrium, Gadolinium or Dysprosium. Scripta Materialia 2003;48:1023-28.
[27] Feyerabend F, Fischer J, Holtz J, Witte F, Willumeit R, Drückere H, Vogt C, Hort N. Evaluation of short-term effects of rare earth and other elements used in magnesium alloys on primary cells and cell lines. Acta Biomater. 2010;6:1834-42.
[28] Heinrich MC, Kuhlmann MK, Kohlbacher S, Scheer M, Grgic A, Heckmann MB, Uder M. Cytotoxicity of iodinated and gadolinium-based contrast agents in renal tubular cells at angiographic concentrations: In vitro study. Radiology 2007;242:425-34.
[29] Thomsen HS. Gadolinium-based contrast media may be nephrotoxic even at approved doses. Eur. Radiol. 2004;14:1654-56.
[30] Maiseyeu A, Mihai G, Kampfrath T, Simonetti OP, Sen CK, Roy S, Rajagopalan S, Parthasarathy S. Gadolinium-containing phosphatidylserine liposomes for molecular imaging of atherosclerosis. Journal of Lipid Research 2009;50:2157-63.
[31] Peng Q, Huang Y, Zhou L, Hort N, Kainer KU. Preparation and properties of high purity Mg-Y biomaterials. Biomaterials 2010;31:398-403.
[32] ASTM E112. Standard test methods for determining average grain size. doi: 10.1520/E0112-96R04E02.
[33] Vostry P, Smola B, Stulikova I, von Buch F, Mordike BL. Microstructure evolution in isochronally heat treated Mg-Gd alloys. Physica Status Solidi a-Applied Research 1999;175:491-500.
[34] Honma T, Ohkubo T, Hono K, Kamado S. Chemistry of nanoscale precipitates in Mg-2.1Gd-0.6Y-0.2Zr (at.%) alloy investigated by the atom probe technique. Mater. Sci. Eng. A 2005;395:301-06.
[35] DIN EN ISO 10002. Tension testing of metallic materials. Berlin, Germany: Beuth Verlag; 2001.
[36] DIN 50106. Compression testing of metallic materials. Berlin, Germany: Beuth Verlag;1978.

[37] ASTM G31-72. Standard Practice for Laboratory Immersion Corrosion Testing of Metals. 2004, DOI: 10.1520/G0031-12A.
[38] Nie JF, Muddle BC. Characterisation of strengthening precipitate phases in a Mg-Y-Nd alloy. Acta Materialia 2000;48:1691-703.
[39] Liang S, Guan D, Tan X, Chen L, Tang Y. Effect of isothermal aging on the microstructure and properties of as-cast Mg-Gd-Y-Zr alloy. Mater. Sci. Eng. A 2011;528:1589-95.
[40] Antion C, Donnadieu P, Tassin C, Pisch A. Early stages of precipitation and microstructure control in Mg-rare earth alloys. Philosophical Magazine 2006;86:2797-810.
[41] Song G, StJohn D. The effect of zirconium grain refinement on the corrosion behaviour of magnesium-rare earth alloy MEZ. Journal of Light Metals 2002;2:1-16.
[42] HE F, Mordike BL. Magnesium Technology - Metallurgy, Design Data, Applications. Berlin, Germany: Springer, 2006.
[43] Qian M, Zheng L, Graham D, Frost MT, StJohn DH. Settling of undissolved zirconium particles in pure magnesium melts. Journal of Light Metals 2001;1:157-65.
[44] Nayeb-Hashemi AA, Clark JB. Phase Diagram of Binary Magnesium Alloys. Metal Park, OH, USA: ASM International, 1988.
[45] Apps PJ, Karimzadeh H, King JF, Lorimer GW. Phase compositions in magnesium-rare earth alloys containing yttrium, gadolinium or dysprosium. Scripta Materialia 2003;48:475-81.
[46] Xu Y, Chumbley LS, Weigelt GA, Laabs FC. Analysis of interdiffusion of Dy, Nd, and Pr in Mg. J. Mater. Res. 2001;16:3287-92.
[47] Nie JF. Effects of precipitate shape and orientation on dispersion strengthening in magnesium alloys. Scripta Materialia 2003;48:1009-15.
[48] Liang S, Guan D, Tan X. The relation between heat treatment and corrosion behavior of Mg-Gd-Y-Zr alloy. Mater. Des. 2011;32:1194-99.
[49] Peng LM, Chang JW, Guo XW, Atrens A, Ding WJ, Peng YH. Influence of heat treatment and microstructure on the corrosion of magnesium alloy Mg-10Gd-3Y-0.4Zr. Journal of Applied Electrochemistry 2009;39:913-20.
[50] Liu CL, Wang YJ, Zeng RC, Zhang XM, Huang WJ, Chu PK. In vitro corrosion degradation behaviour of Mg–Ca alloy in the presence of albumin. Corros. Sci. 2010;52:3341-47.
[51] Mueller W-D, Fernandez Lorenzo de Mele M, Nascimento ML, Zeddies M. Degradation of magnesium and its alloys: Dependence on the composition of the synthetic biological media. J. Biomed. Mater. Res. 2009;90A:487-95.
[52] Zainal Abidin NI, Martin D, Atrens A. Corrosion of high purity Mg, AZ91, ZE41 and Mg2Zn0.2Mn in Hank's solution at room temperature. Corros. Sci. 2011;53:862-72.
[53] Kirkland NT, Lespagnol J, Birbilis N, Staiger MP. A survey of bio-corrosion rates of magnesium alloys. Corros. Sci. 2010;52:287-91.
[54] Moravej M, Purnama A, Fiset M, Couet J, Mantovani D. Electroformed pure iron as a new biomaterial for degradable stents: In vitro degradation and preliminary cell viability studies. Acta Biomaterialia, The THERMEC 2009 Biodegradable Metals 2010;6:1843-51.
[55] Hermawan H, Purnama A, Dube D, Couet J, Mantovani D. Fe-Mn alloys for metallic biodegradable stents: Degradation and cell viability studies. Acta Biomaterialia, The THERMEC 2009 Biodegradable Metals 2010;6:1852-60.
[56] Liu B, Zheng YF. Effects of alloying elements (Mn, Co, Al, W, Sn, B, C and S) on biodegradability and in vitro biocompatibility of pure iron. Acta Biomater. 2011;7:1407-20.

[57] Peuster M, Hesse C, Schloo T, Fink C, Beerbaum P, von Schnakenburg C. Long-term biocompatibility of a corrodible peripheral iron stent in the porcine descending aorta. Biomaterials 2006;27:4955-62.
[58] Peuster M, Wohlsein P, Brugmann M, Ehlerding M, Seidler K, Fink C, Brauer H, Fischer A, Hausdorf G. A novel approach to temporary stenting: Degradable cardiovascular stents produced from corrodible metal - Results 6-18 months after implantation into New Zealand white rabbits. Heart 2001;86:563-69.

Figure captions

Fig. 1. Optical microstructure of the DG28K alloy in the: (a) as-cast condition; (b) T4 condition.

Fig. 2. Grain size of Mg-10(Dy+Gd)-0.2Zr alloys in as-cast and T4 conditions.

Fig. 3. SEM microstructure of the as-cast alloys: (a) D10K; (b) DG82K; (c) DG55K; (d) DG28K.

Fig. 4. SEM microstructure of alloys after T4 treatment: (a) D10K; (b) DG82K; (c) DG55K; (d) DG28K.

Fig. 5. Age hardening response of Mg-10(Dy+Gd)-0.2Zr alloys at 200 °C.

Fig. 6. TEM micrograph showing the precipitates distribution and the corresponding diffraction patterns of DG28K alloy in peak-aged condition (200°C / 72 h). The electron beam is parallel to: (a, b) $\langle \bar{1}2\bar{1}3 \rangle_{\alpha}$; (c, d) $[0001]_{\alpha}$.

Fig. 7. XRD of DG28K alloy in different conditions.

Fig. 8. Mechanical properties of Mg-Dy-Gd-Zr alloys: (a) tensile yield strength; (b) ultimate tensile strength; (c) elongation; (d) compressive yield strength; (e) ultimate compressive strength; (f) compressibility (strain at maximum stress point).

Fig. 9. Corrosion rate of Mg-10(Dy+Gd)-0.2Zr alloys after immersion in CCM for 14 days under cell culture conditions.

Fig. 10. Macro corrosion morphology of Mg-10(Dy+Gd)-0.2Zr alloys after 14 days immersion in CCM under cell culture conditions (after removal of corrosion products).

Fig. 11. Mg rich side of binary (a) Mg-Dy and (b) Mg-Gd phase diagrams (wt.%) [44].

Table captions

Table 1 Nominal chemical composition of experimental alloys (wt.%).

Table 2 Experimentally measured chemical composition of Mg-10(Dy+Gd)-0.2Zr alloys (wt.%).

Table 3 Distribution of alloying elements in various region of the as-cast Mg-10(Dy+Gd)-0.2Zr alloys (wt.%), analyzed by EDX.

Table 4 Difference in mechanical properties in T4 to T6 (peak aged) conditions.

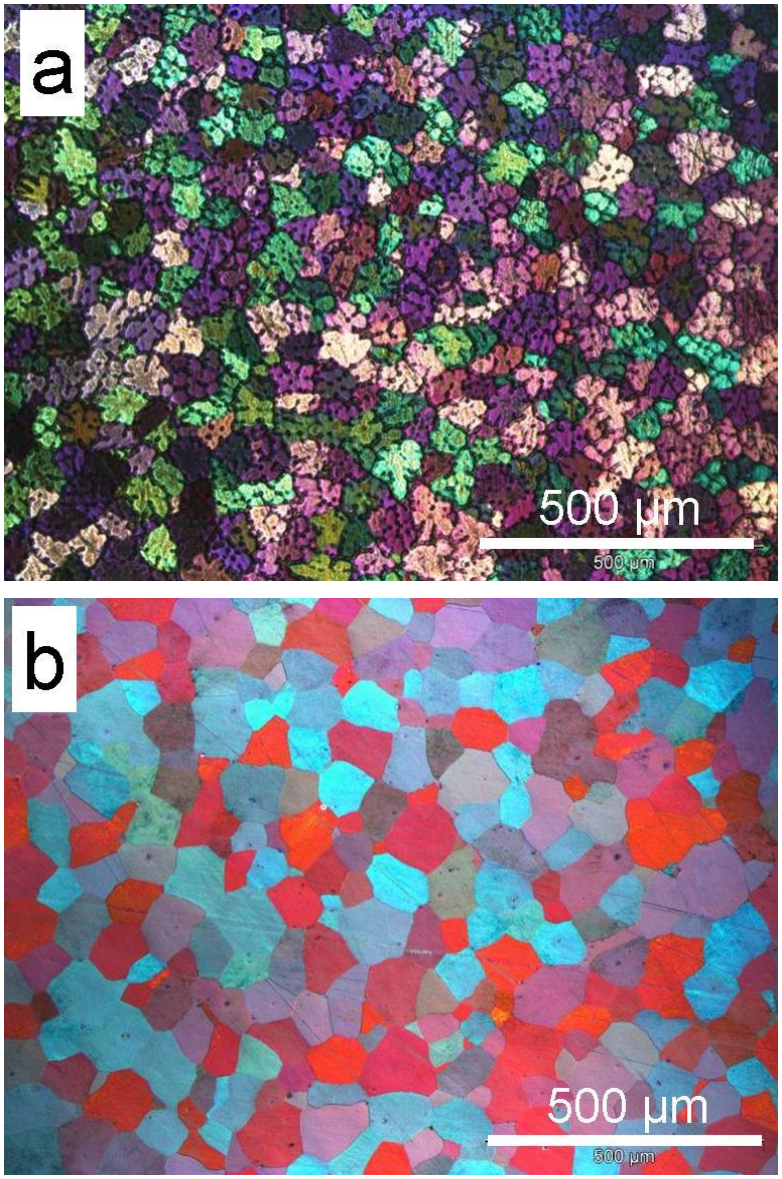

Fig. 12. Optical microstructure of DG28K alloys: (a) as-cast condition; (b) T4 condition.

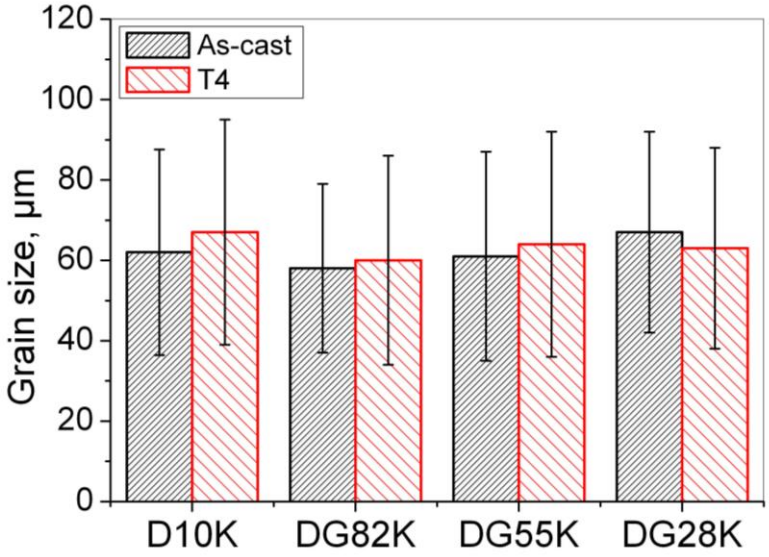

Fig. 13. Grain size of alloys in as-cast and T4 conditions.

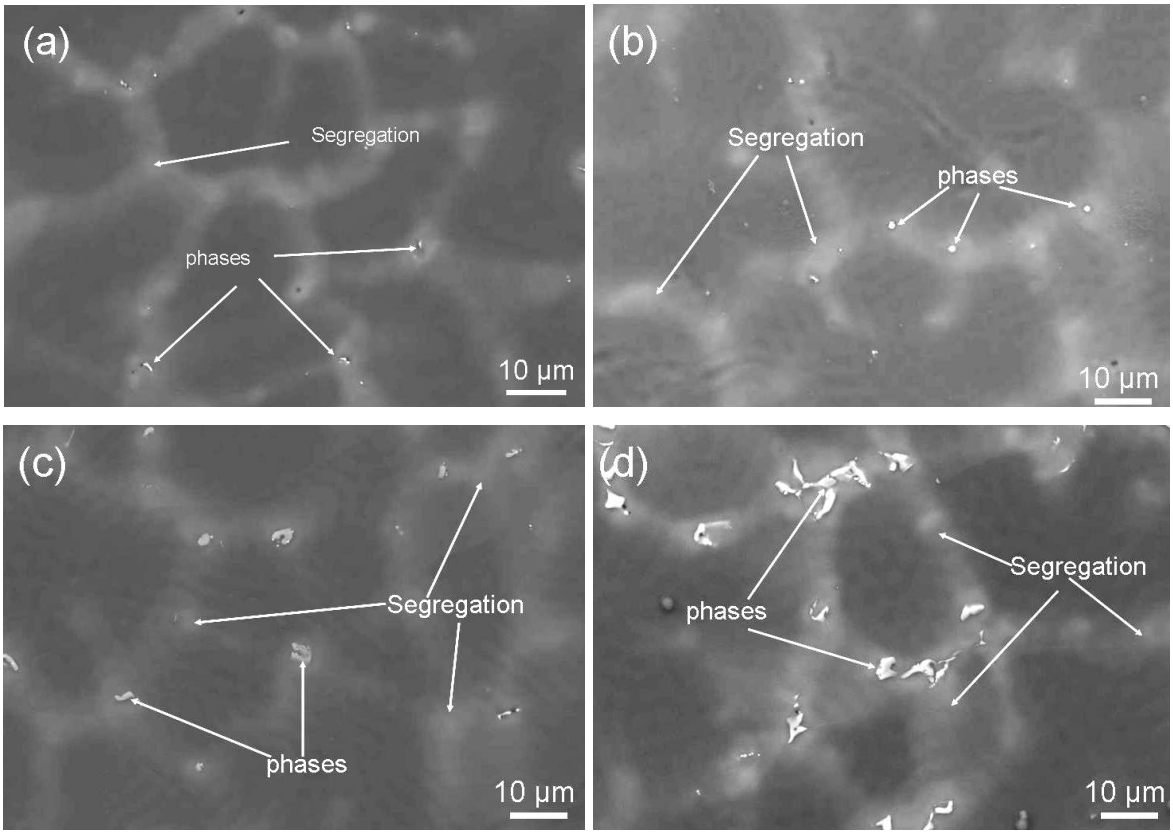

Fig. 14. SEM microstructure of as-cast alloys: (a) D10K; (b) DG82K; (c) DG55K; (d) DG28K.

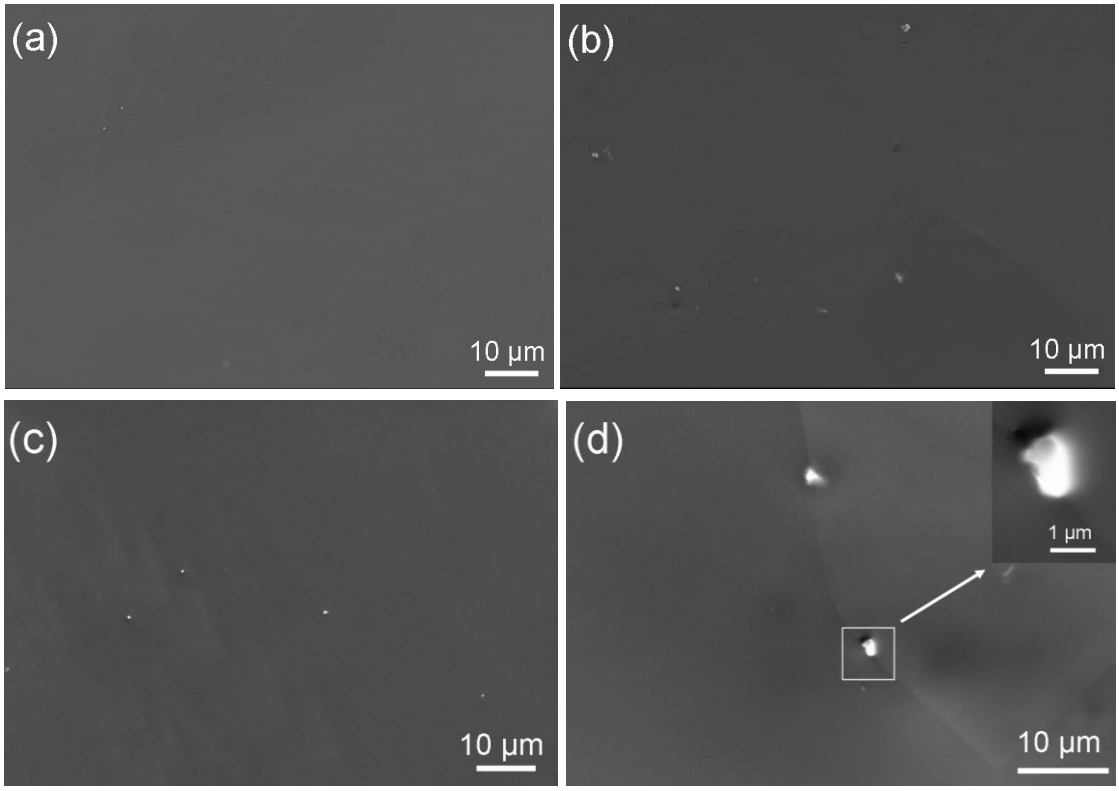

Fig. 15. SEM microstructure of alloys after T4 treatment: (a) D10K; (b) DG82K; (c) DG55K; (d) DG28K.

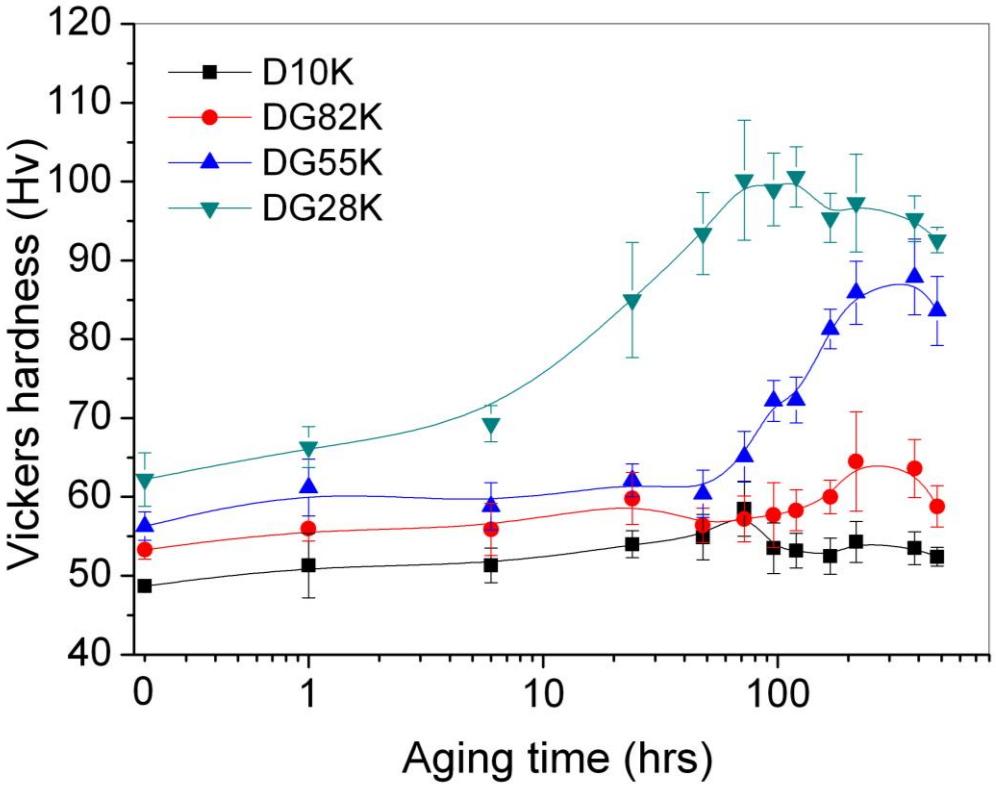

Fig. 16. Age hardening response of Mg-10(Dy+Gd)-0.2Zr alloys at 200 °C.

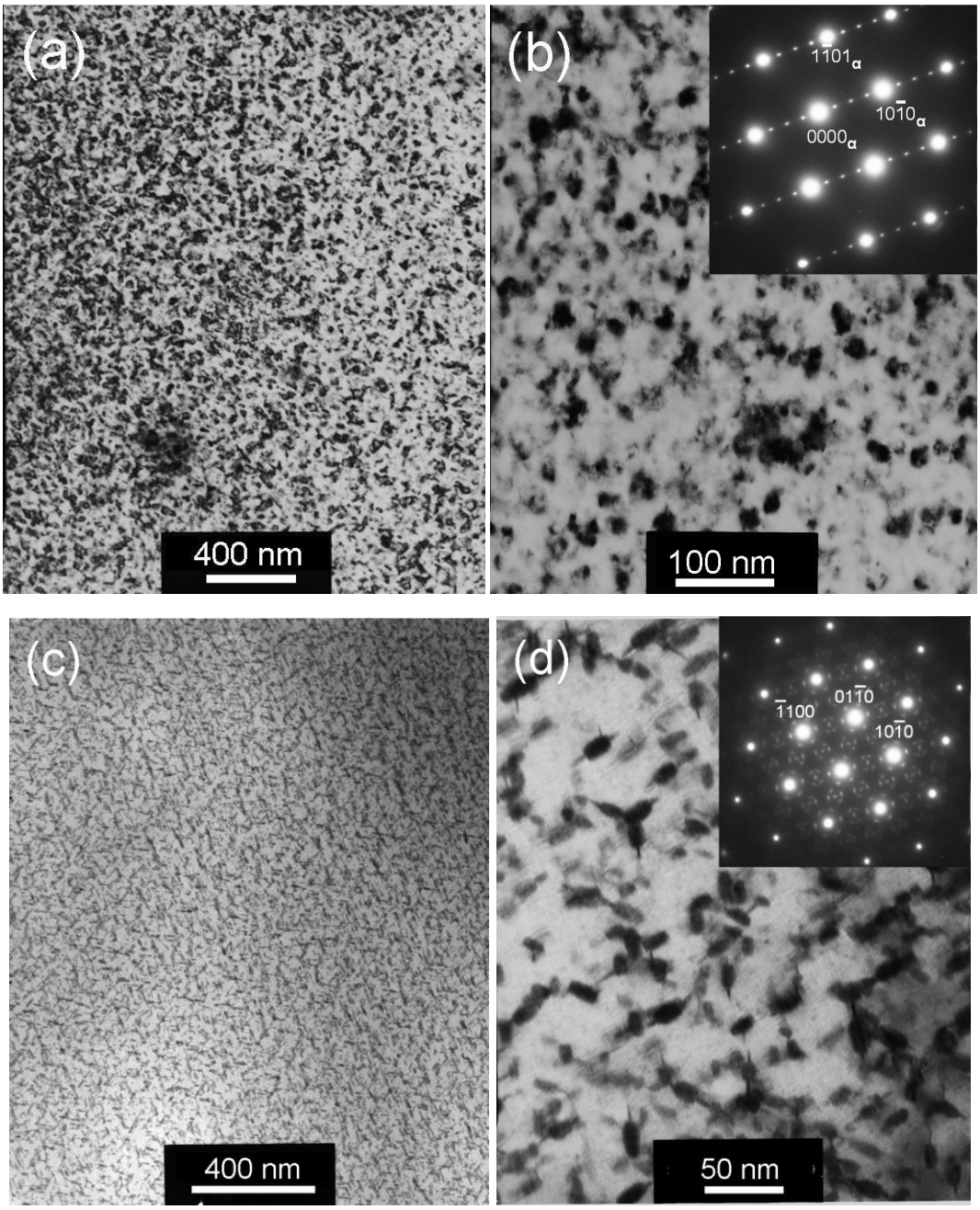

Fig. 17. TEM micrograph showing the precipitates distribution and the corresponding diffraction patterns of DG28K alloy in peak-aged condition (200°C / 72 h). The electron beam is parallel to: (a, b) $[\bar{1}2\bar{1}3]\alpha$; (c, d) $[0001]\alpha$.

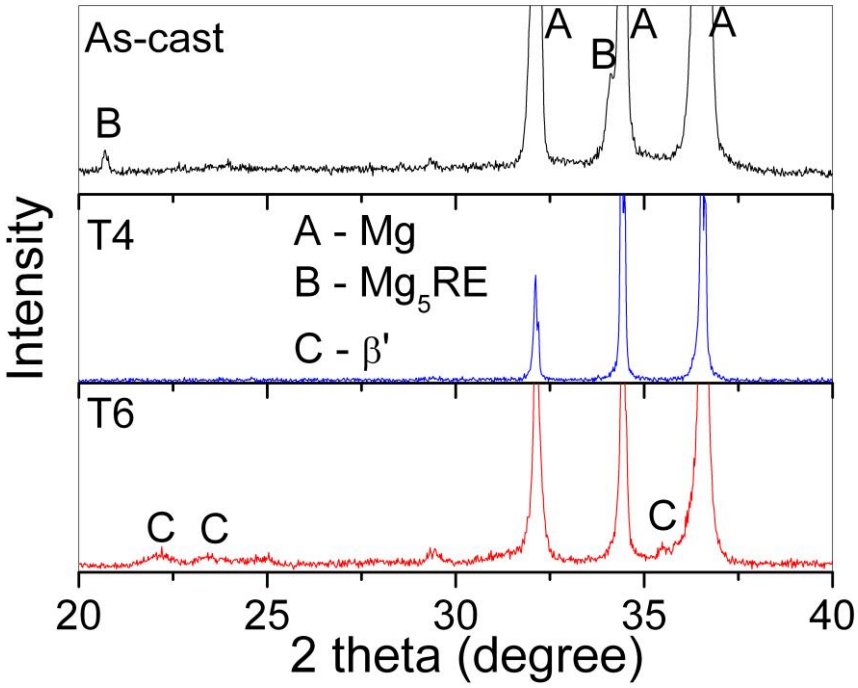

Fig. 18. XRD of DG28K alloy in different conditions.

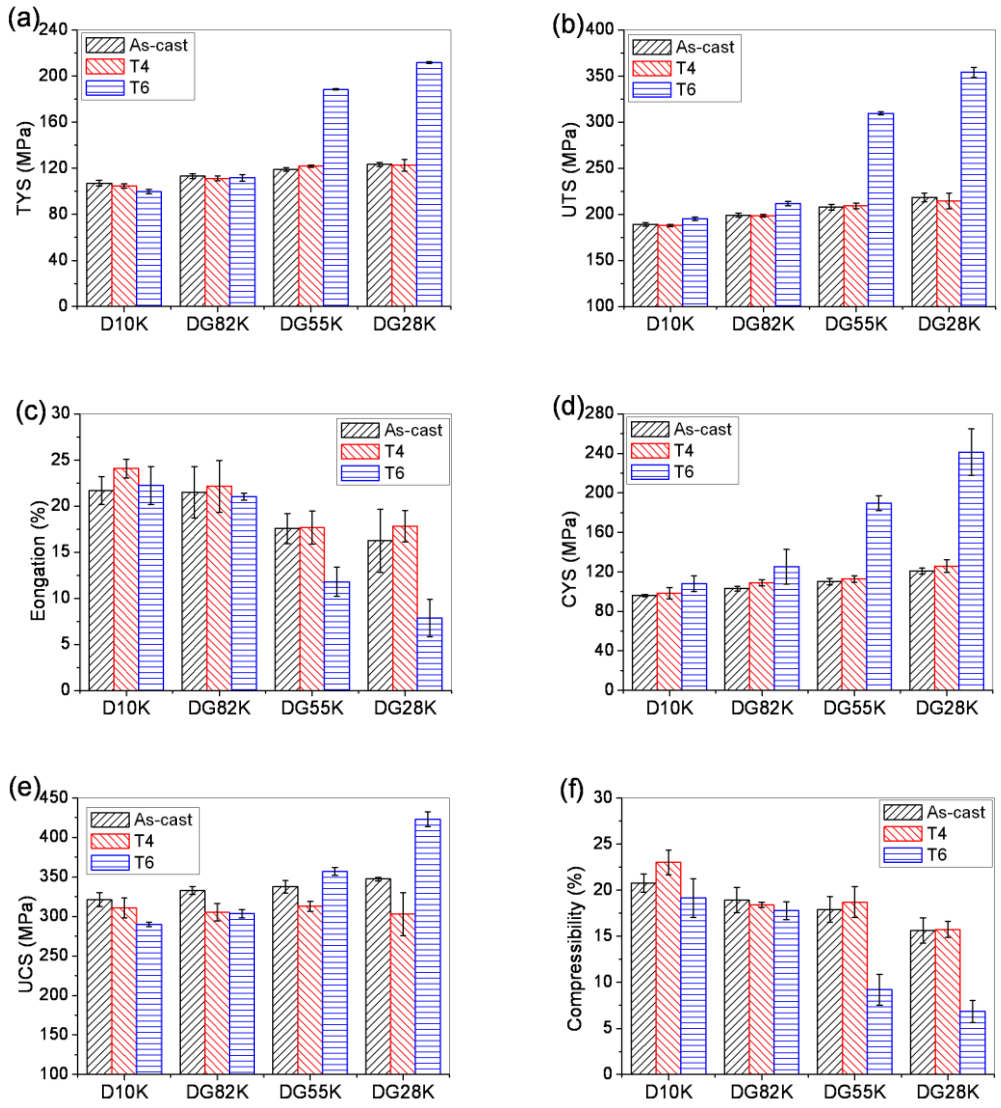

Fig. 19. Mechanical properties of Mg-Dy-Gd-Zr alloys: (a) tensile yield strength; (b) ultimate tensile strength; (c) elongation; (d) compression yield strength; (e) ultimate compression strength; (f) compressibility (strain at maximum stress point).

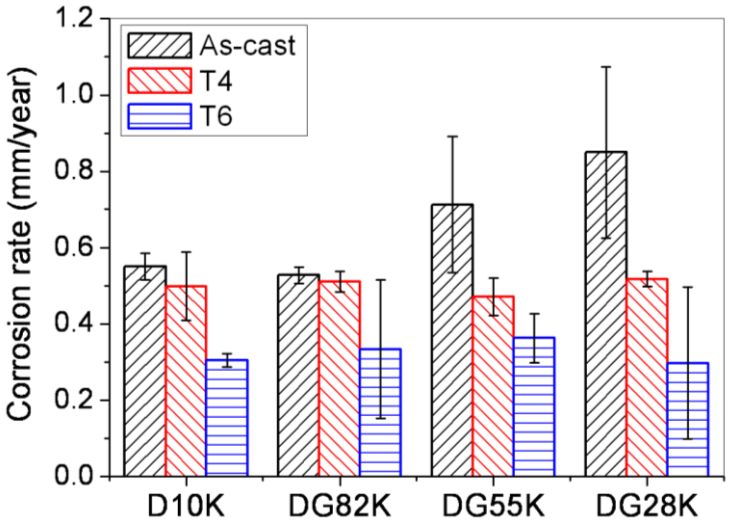

Fig. 20. Corrosion rate of alloys after immersion in CCM for 14 days under cell culture conditions.

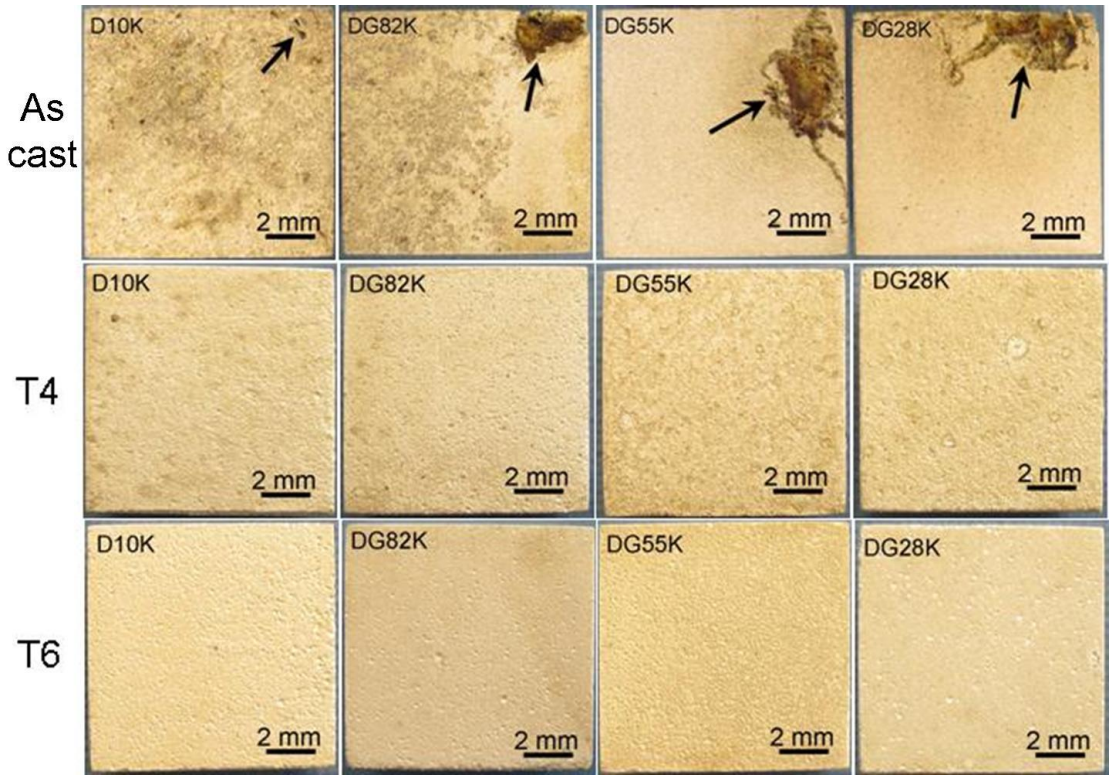

Fig. 21. Macro corrosion morphology of alloys after 14 days immersion in CCM under cell culture conditions (after removal of corrosion products).

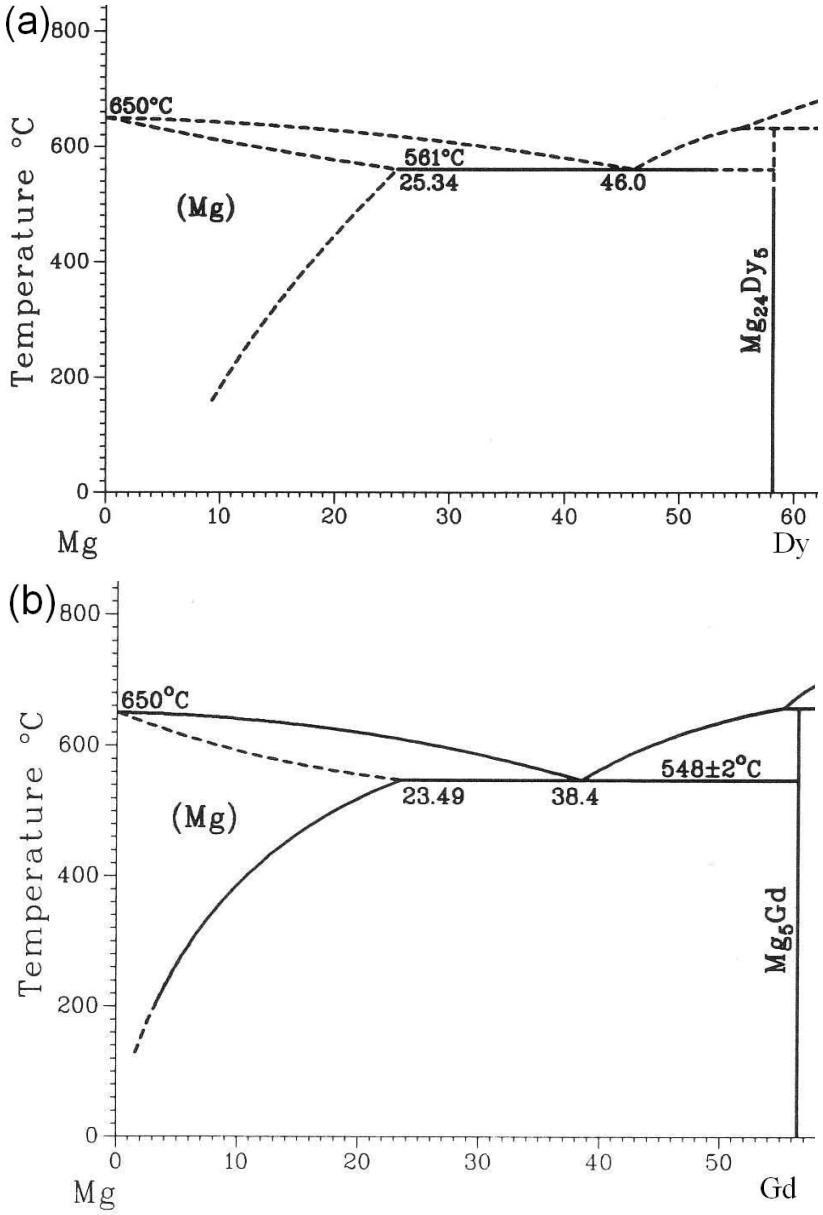

Fig. 22. Mg rich side of binary (a) Mg-Dy and (b) Mg-Gd phase diagrams (wt.%) [43].

Table 5 Nominal chemical composition of experimental alloys (wt.%).

alloys	code	Dy	Gd	Zr	Mg
Mg-10Dy-0.2Zr	D10k	10		0.2	Balance
Mg-8Dy-2Gd-0.2Zr	DG82K	8	2	0.2	Balance
Mg-5Dy-5Gd-0.2Zr	DG55K	5	5	0.2	Balance
Mg-2Dy-8Gd-0.2Zr	DG28K	2	8	0.2	Balance

Table 6 Experimentally measured chemical composition of Mg-10(Dy+Gd)-0.2Zr alloys (wt.%).

alloys	code	Dy	Gd	Zr	Fe	Ni	Cu	Mg
Mg-10Dy-0.2Zr	D10k	8.74	--	0.033	0.002	<0.004	0.004	Balance
Mg-8Dy-2Gd-0.2Zr	DG82K	7.08	1.57	0.037	0.002	<0.004	0.004	Balance
Mg-5Dy-5Gd-0.2Zr	DG55K	4.28	4.09	0.026	0.001	<0.004	0.004	Balance
Mg-2Dy-8Gd-0.2Zr	DG28K	1.60	7.24	0.030	0.003	<0.004	0.006	Balance

Table 7 Distribution of alloying elements in various region of as-cast Mg-10(Dy+Gd)-0.2Zr alloys (wt.%), analyzed by EDX.

alloys	Dy (matrix)	Gd (matrix)	Dy (segregation)	Gd (segregation)	Dy (phase)	Gd (phase)
D10K	4.08±0.26	--	19.6±0.73	--	--	--
DG82K	3.27±0.11	0.68±0.08	14.8±1.61	4.1±0.64	--	--
DG55K	2.24±0.38	1.52±0.23	8.77±0.57	8.16±0.85	14.6±0.81	32.5±1.8
DG28K	1.03±0.06	2.36±0.14	3.3±0.17	12.2±0.34	6.74±0.25	44.1±1.82

Table 8 Difference in mechanical properties in T4 to T6 (peak aged) conditions.

condition	alloy	TYS	UTS	Elong.	CYS	UCS	Comp. Duct.
(T6-T4)	D10K	-4.8	7.3	-1.9	9.8	-20.9	-3.9
	DG82K	0.5	13.3	-1.1	16.1	-1.8	-0.7
	DG55K	66.5	100.3	-5.8	76.9	44.4	-9.5
	DG28K	89.1	139.3	-10	115.4	120.1	-8.9